ACS APPLIED MATERIALS & INTERFACES

Research Article

www.acsami.org

Synthesis of Nanoparticles from Malleable and Ductile Metals Using Powder-Free, Reactant-Assisted Mechanical Attrition

Brandon W. McMahon,[†] Jesus Paulo L. Perez,[†] Jiang Yu,[†] Jerry A. Boatz,[‡,§] and Scott L. Anderson*[,†,§]

[†]Chemistry Department, University of Utah, 315 South 1400 East, Salt Lake City, Utah 84112, United States

[‡]Propellants Branch, Rocket Propulsion Division, Aerospace Systems Directorate, Air Force Research Laboratory, AFMC AFRL/RQRP, 10 East Saturn Boulevard, Edwards AFB, California 93524, United States

Supporting Information

ABSTRACT: A reactant-assisted mechanochemical method was used to produce copious nanoparticles from malleable/ductile metals, demonstrated here for aluminum, iron, and copper. The milling media is intentionally degraded via a reactant-accelerated wear process, where the reactant aids particle production by binding to the metal surfaces, enhancing particle production, and reducing the tendency toward mechanochemical (cold) welding. The mechanism is explored by comparing the effects of different types of solvents and solvent mixtures on the amount and type of particles produced. Particles were functionalized with oleic acid to aid in particle size separation, enhance dispersion in hydrocarbon solvents, and protect the particles from oxidation. For aluminum and iron, the result is air-stable particles, but for copper, the suspended particles are found to dissolve when exposed to air. Characterization was performed using electron microscopy, dynamic light scattering, Fourier transform infrared spectroscopy, solid state nuclear magnetic resonance, and X-ray photoelectron spectroscopy. Density functional theory was used to examine the nature of carboxylic acid binding to the aluminum surface, confirming the dominance of bridging bidentate binding.

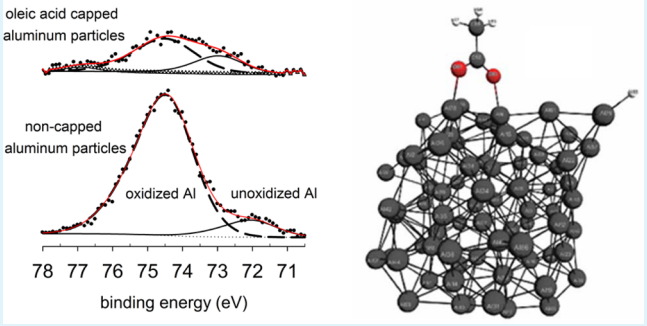

KEYWORDS: *milling, wear, nanoparticle synthesis, aluminum, copper, iron, mechanochemistry*

1. INTRODUCTION

Ball milling and related methods provide efficient means for particle production from bulk starting materials, and in the case of brittle materials, size reduction into the sub-100 nm range is possible.[1−3] The resulting size distribution is determined by the balance between fracturing to create smaller particles and mechanochemical "cold" welding, which tends to build up larger particles.[4,5] In a typical approach, micron or larger scale powder might be milled together with balls or other milling media of some hard material such as tungsten carbide, thereby being fractured into finer particles. For ductile and malleable materials, this approach can be inefficient, both because the particles are not readily fractured and because mechanochemical welding is relatively efficient.[6,7]

Here, we discuss a reactant-assisted mechanical attrition process, which efficiently generates nanoparticles from malleable and ductile metals, via reactant-accelerated wear of particles from the surfaces of balls or other media composed of the metal of interest. The process quickly and simply generates grams of nanoparticles using inexpensive feedstock in a laboratory-scale mill, while simultaneously coating the particles with a protective ligand. The milling process should be adaptable to larger scale production and thus provide a useful method for generating particles for application where large quantities of particles with controlled surface chemistry are required, such as high energy density propellant additives or water remediation agents.[8,9] This style of mechanical attrition also largely avoids an issue with conventional ball milling—which the products tend to become contaminated by material abraded or fractured from the milling media or jar walls, with contaminant levels increasing with milling time. Because the media is composed of the material of interest, which is softer than the milling vessel walls, contaminant levels are low.

The focus of this report is on understanding the mechanisms involved in the reactant-assisted nanoparticle production process and on optimizing conditions for production of particles, by controlling the particle surface chemistry. Particle production is explored in detail for the case of aluminum, which is not efficiently reduced to small nanoparticles in conventional ball milling.[10] The effects of different solvents and additives are used to probe the mechanism of particle production. The generality of mechanically attriting parent media to form nanoparticles is demonstrated by application to production of iron and copper nanoparticles.

The use of liquid reactants/adsorbates to enhance fracturing and wear has been examined for decades, since the early work

Received: June 16, 2014
Accepted: October 24, 2014
Published: October 24, 2014

of P. A. Rehbinder.[11] Nascent metal surfaces generated by fracturing have relatively high surface free energies,[7,12] adsorption of a strongly binding reactant lowers the energy, enhancing fracturing, and also reducing the tendency toward particle aggregation and cold welding.[12,13] Westwood et al.[14] discovered that the hardness of a material is at its maximum when the charge at the surface of the material is at a minimum (i.e., zero). Gayko et al.[15] reported a study that is probably the most closely related to what we are reporting here. They demonstrated the effects of adsorbates on size reduction in milling of aluminum powder with steel balls assisted by a variety of solvents. They discovered that the resulting size distribution shifted to smaller sizes when aluminum was milled in solvents that might be expected to adsorb strongly to aluminum (e.g., nitriles, alcohols, ketones), as opposed to solvents, such as hydrocarbons, which might be expected to interact weakly with the surface. Their study did not examine particles smaller than 20 μm, did not attempt to explore the effects of metal surface oxidation, and did not include measurements of the mode of adsorbate−surface binding. Here, we report a study that is focused on nanoparticle production, including spectroscopic and theoretical characterization of the resulting particle surfaces, and which examines the effects of surface oxidation and use of surface functionalization to control dispersibility in various solvents, both as a means to prepare stable suspensions, and to aid in size-separation. In particular, we demonstrate production of Al, Fe, and Cu nanoparticles capped in situ with oleic acid, to generate particles that are dispersible in hydrocarbons. Such particles are of interest as additives to hydrocarbon fuels.[16−22]

2. MATERIALS AND METHODS

2.1. Safety Considerations. The process described below has the potential to generate large quantities of unprotected, oxidizable nanoparticles, which spontaneously ignite upon exposure to air, water or other reactive species. All handling of milling feedstock and products is done inside an inert atmosphere glovebox, and milling is done in a sealed jar, pressurized with inert gas to minimize air intrusion. Caution must also be exercised in choice of milling solvents and reactants. Some, such as alcohols or organic acids, may contain functional groups that react with the surfaces of the nascent nanoparticles, generating large volumes of hydrogen or other gases, which can pressurize the milling vessel to several atmospheres. We have also seen some evidence for HCN production in milling of reactive metals with nitrile-containing solvents. For safety, initial trials involving new reagents should be limited in volume, such that complete decomposition to gaseous products would not overpressurize the milling vessel. Because of the potential for generation of reactive or toxic gases, provision should be made for controlled venting of the milling vessel, before the vessel is opened in an inert atmosphere, as described below.

2.2. Milling Methodology. Particle production was done using a Retsch PM 400 planetary ball mill, and Retsch 250 mL tungsten carbide jars with custom-fabricated 316 stainless steel lids (Supporting Information Figure S1). The lids have the same dimensions as the original Retsch lids but have a pair of threaded ports equipped with valves (McMaster-Carr part number 4912K96) that serve several purposes. The jars are loaded and sealed inside a N_2-filled glovebox, which is equipped with a vacuum/pressure manifold that can be attached to the valves in the jar lid. To avoid potential reaction of N_2 with the nanoparticles under milling conditions, the manifold is used to pump out the N_2 after the jar is closed and then backfill the jar with Argon (99.9999%) prior to milling. The manifold has a pressure/vacuum gauge that can be used for leak detection, and to check the jar pressure after milling. Milling solvents were degassed using a freeze−pump−thaw procedure and stored in the glovebox with activated 5 Å molecular sieves to remove any dissolved water. Solutions can be introduced into the jar via the valves by evacuating the jar with one valve and drawing the solution in through the other valve. After filling, the sealed jar was removed from the glovebox and loaded into the mill. To allow direct comparison of different milling mixtures, all samples were prepared using identical milling parameters: 3 h milling at 350 rpm sun wheel rotational frequency, corresponding to ∼21 g relative centrifugal force. The temperature of the jar rises during the course of milling, reaching a maximum of ∼105 °C, presumably enhancing the rates of reactions of the milling liquids with the metal surfaces. After milling, the jar was reintroduced into the glovebox and attached to the pressure/vacuum manifold, allowing the headspace to be evacuated and exhausted into a fume hood. The jar was then opened in the N_2 atmosphere and the contents were removed, with particles washed from the milling media using an appropriate solvent.

2.3. Aluminum Nanoparticle Synthesis. Because aluminum is highly malleable and reactive, efficient production of aluminum particles is not straightforward, and many permutations of solvents and capping agent concentrations were investigated to provide insight into the factors that control efficiency of particle production by this technique. Aluminum milling was done using ∼200 g of 8 mm aluminum balls and 100 mL of various solvent mixtures. After adding the balls, the jar was evacuated and purged, the solvent mixture was drawn into the jar, and finally, the jar was pressurized with argon before being transferred out of the glovebox for milling. All solvents were degassed by freeze−pump−thaw cycles and stored in the glovebox over molecular sieves.

The solvent that gave the best nanoparticle production was acetonitrile. In a typical process, aluminum balls were milled in 100 mL of acetonitrile for 3 h at 350 rpm, generating copious particles, forming a dense slurry. For some experiments, the particles generated in acetonitrile were subsequently reacted with oleic acid to render them hydrocarbon-dispersible. For this purpose, we simply added oleic acid (3 mL) to the aluminum-acetonitrile slurry in the milling jar, and then milled it for 15 min at 100 rpm to thoroughly mix the oleic acid into the aluminum-containing slurry, while minimizing production of additional particles. After interaction with oleic acid, the particles no longer were dispersible in acetonitrile, and precipitated out, allowing the acetonitrile to be decanted from the jar. The particles were found to be highly dispersible in hydrocarbons, and therefore, *n*-hexane was used to wash the particles out of the jar. Results for additional solvents and solvent mixtures are discussed below.

2.4. Unoxidized Iron Nanoparticle Synthesis. Iron nanoparticles were generated by milling 3 mm diameter mild steel balls. Approximately 200 g of balls were loaded into the milling jar, which was then evacuated and purged with argon several times. The jar was then evacuated again, and 100 mL of 5% oleic acid in *n*-hexane was drawn into the jar, before it was finally pressurized again with 55 psia of argon. The loaded jar was then milled at 350 rpm for 3 h.

2.5. Oxidized Iron Nanoparticle Synthesis. To produce oxidized iron nanoparticles, the jar was loaded with 200 g of

Table 1. Results for Milling in Nonpolar Solvents and Oleic Acid Solutions in Nonpolar Solvents[a]

particles produced using nonpolar solvent	benzene	*n*-heptane	toluene	1.7×10^{-5} M OA in toluene	3.0×10^{-5} M OA in toluene	1.0×10^{-2} M OA in toluene	*n*-hexane	1.6×10^{-1} M OA in hexane
nanoparticles	x	x	x	x	x	~10 mg	x	~100 mg
micron flakes	x	x	x	~10 mg	~23 mg	~500 mg	x	~1 g

[a]Note: x indicates that <1 mg produced.

Table 2. Particle Production Results for Milling in Various Polar Solvents

particles produced using polar solvent	oleic acid	oleylamine	benzylamine	acetonitrile	ethanol	dichloromethane
nanoparticles	~100 mg	~10 mg	~10 mg	~1 g	~5 g Al_2O_3	~5 g $AlCl_3$
micron flakes	~5 g	~2 g	~3 g	~1 g		

steel balls and 100 mL of 5% oleic acid in *n*-hexane and then sealed outside the glovebox, with 1 atm of laboratory air as the headspace atmosphere. This sample was also milled at 350 rpm for 3 h.

2.6. Copper Nanoparticle Synthesis. Because we were unable to find inexpensive copper spheres, we tested production of copper particles by using copper cylinders fabricated by simply cutting 6.35 mm diameter copper rod into a roughly 6 mm segments. The jar was filled with ~200 g of copper cylinders and 100 mL of a 5% oleic acid solution in *n*-hexane using the evacuation and argon purging method described above, then milled for 3 h at 350 rpm.

3. ANALYSIS

Particle sizes were characterized by a combination of electron microscopy and dynamic light scattering (DLS). DLS was performed using a NICOMP 380 ZLS instrument, with samples prepared by sonication in *n*-hexane for 30 min to disperse particles and break up aggregates. The concentration of the samples was adjusted by diluting in *n*-hexane until the dispersion was only slightly turbid. Size distributions were taken as the average of results from two 5 min runs.

Scanning electron microscopy (SEM) was done using an FEI Nova Nano 600 instrument. Scanning transmission electron microscopy (STEM) was performed using an FEI Titan instrument operated at 200 kV. Samples were prepared for microscopy analysis using the same dispersion/dilution procedure used in DLS, with the exception that samples were ultrasonicated just before drop casting on lacey carbon transmission electron microscopy (TEM) grids.

Fourier transform infrared (FTIR) spectroscopic experiments were performed using a Bruker Tensor 37 instrument, modified to collect light specularly reflected from the samples. The samples were drop casted onto a stainless steel stub, light from the IR source was focused onto the sample using an off-axis paraboloid, and light reflected from the sample was collected and refocused onto a mercury−cadmium−telluride detector with a spectral range of 4000 cm^{-1} to 850 cm^{-1}. The sample thickness was sufficient that the stainless steel stub was completely covered.

X-ray photoelectron spectroscopy (XPS) was performed on a Kratos Axis Ultra instrument, using monochromatic Al Kα radiation (1486.6 eV) and an analysis area of 300 × 700 μm. Samples were prepared by drop casting onto stainless steel shims, and drying in air. Samples were placed in the instrument load-lock chamber and evacuated for a minimum of 12 h by a turbo pump, to remove any volatile materials trapped in the sample matrix prepared by drop casting. Charging of the sample under X-ray irradiation was compensated using a low energy electron flood gun, tuned to optimize the sharpness of the XPS peaks. Spectra were analyzed using the Casa XPS program, and the binding energy scale was corrected to put the adventitious sp^2 carbon peak at 284.8 eV.[23−25]

Solid-state nuclear magnetic resonance was performed on aluminum nanoparticles functionalized with acetic acid. Acetic acid was chosen as a simple carboxylic acid to avoid complications from using oleic acid. A sample of the acetic acid-capped particles was loaded into a 5 mm ceramic SSNMR rotor kit (ceramic sleeve, delrin drive tip, Teflon plugs and spacers). The sample was mounted in a 5 mm SSNMR probe with the sample orientation fixed at the "magic angle", for example, 54.7 degrees with respect to the main field (Zeeman) axis. The ^{13}C NMR spectrum of the capped particles was recorded using a standard cross-polarization/magic-angle-spinning experiment (CP/MAS), spinning at 3000 Hz. The ^{13}C and ^{1}H carrier frequencies were 50.305 and 200.044 MHz, respectively. The CP contact time was 3 ms. The ^{13}C spectral width was 20 kHz and the acquisition time was 51 ms. A three second delay between pulses was used to achieve near-equilibrium magnetization between excitations. All of the parameters used are standard for samples of this type.

To help understand the nature of oleic acid-aluminum binding, the interactions between aluminum nanoparticles and CH_3COOH were computed using density functional theory (DFT) methods with the M06 hybrid meta-generalized gradient approximation (GGA) exchange-correlation functional of Zhao and Truhlar.[26] The McLean−Chandler (12s,9p)/[6s,5p] contracted basis set,[27] augmented with a d-type polarization function[28] and diffuse s+p shell,[29] was used for aluminum and the 6-311++G(d,p) basis set[29,30] was used for carbon, oxygen, and hydrogen, with this combination of functional and basis sets henceforth denoted simply as M06/6-311++G(d,p). A cluster of 80 aluminum atoms, derived from a previously reported[31] calculated geometry of an 80-atom boron cluster with both exposed surface atoms and a bulk-like core, was used as a model for an aluminum nanoparticle. All structures reported herein were fully optimized and have been calculated to be local minima via diagonalization of the Hessian matrix. All calculations were performed using the GAMESS[32] quantum chemistry program.

4. RESULTS AND DISCUSSION

4.1. Aluminum Nanoparticles. In the process of optimizing aluminum nanoparticle production rates, many solvent/reactant mixtures were tried. Because they provide insight into the mechanism for particle production under these initially powder-free conditions, these initial results are summarized here. All aluminum milling was done in argon

atmosphere, and all production methods described below used a liquid solvent or reactant, sometimes alone, and sometimes with oleic acid dissolved. In addition, in some experiments, particles were produced in a pure solvent and subsequently functionalized with oleic acid.

With the addition of an appropriate solvent, significant particle production can be observed, however, the amount and type of particles generated are strongly dependent on the milling mixture. The results of milling in 14 different solvents or mixtures are summarized in Tables 1 and 2. As reviewed by Bowmaker,[33] there are several working theories, but no agreed upon mechanism, for solvent-assisted mechanochemistry, reflecting the difficulties in obtaining molecular-level information under chaotic reaction conditions. The variations seen for different solvents provide some insight, as discussed below.

Consider particle generation in several distinctly different classes of solvents or solvent mixtures, in each case milling 200 g aluminum balls in 100 mL of liquid for 3 h at 350 rpm. As shown in Table 1, when milling in neat hydrocarbons, including both aliphatic and aromatic solvents, no detectable nanoparticles are produced. If these solvents are poured out of the mill into a sample container, the liquid is clear, and the only sign that milling occurred is the presence of a few large silvery flakes with dimensions in the >50 μm size range. See Supporting Information Figure S2a. If the balls milled were initially rough, up to ∼5 mg of flakes might be produced, while initially smooth balls produce only <1 mg. Presumably, initially rough balls increase the collision friction, but since milling in unreactive solvents also polishes the balls, this is not a useful strategy to enhance particle production.

If Al balls are milled in 100 mL of neat oleic acid, a stable gray-black suspension of particles in oleic acid is recovered (see Supporting Information Figure S2c), which could be separated into ∼5 g of shiny, metallic flakes and ∼100 mg of deep black nanoparticles. The high dispersibility, presumably, is due to some combination of particle surfaces being functionalized and oleic acid's high viscosity (>27 000 μPa·s).[34,35] The high viscosity of neat oleic acid may also play a role in particle reduction. Mori et al.[36] investigated the how particle production varied with the viscosity of a slurry in a tumbling ball mill and found that higher slurry viscosities resulted in the milling media rising higher in the mill before falling back to the bottom of the drum. Since there is a direct relationship between the distance the media fell and the momentum of the media at the moment of impact, it is not surprising that they observed more efficient particle production when using higher viscosity slurries. In our planetary mill, the balls also tumble; however, the movement is under a relative centrifugal force of >20 g. Thus, the fluid viscosity might be expected to play a smaller role.

Partly to test the effect of viscosity, we also examined particle production for various concentrations of oleic acid dissolved in low viscosity hydrocarbons, such as toluene and hexane. Table 1 also lists the results for oleic acid concentration up to 0.16 M = 5% by volume. The production of micro- and nanoparticles was estimated by centrifugation, washing, and drying, as above. For low oleic acid concentrations, only micron-size flakes are produced in measurable quantities, but with increasing concentration, both micro- and nanoparticles are produced in reasonable quantities, with large flakes always dominating, by mass. Since nanoparticle production was similar for 0.16 M oleic acid in hexane and neat oleic acid, solutions with concentrations higher than 0.16 M were not investigated. Because the concentration of oleic acid was low in all these solutions, the viscosity was never close to that of neat oleic acid; thus, we attribute the relatively efficient particle production to reaction of oleate with the particle surface rather than viscosity effects. See below for more on this issue.

It is interesting that oleic acid promotes particle production, because it is often included as an additive in lubricants, with the idea that metal surfaces are thereby coated with a strongly adhering, lubricating aliphatic layer.[37,38] For aluminum, at least, addition of oleic acid clearly greatly accelerates the wear rate, generating copious particles in both the nano and micron size regimes. This result is consistent with the proposal by Rehbinder[11] that adsorbates could lower the surface free energy, which might be expected to enhance surface creation by fracturing. In addition, surface functionalization might be expected to reduce the tendency toward cold welding,[15,39] which tends to heal fractures, and reattachment of particles to the ball surfaces.

In addition to oleic acid and solutions thereof, we examined particle production from milling in a series of polar/reactive solvents, including oleylamine, benzylamine, acetonitrile, ethanol, and dichloromethane, and the results are summarized in Table 2. Neat oleic acid, olyelamine, and benzylamine resulted in qualitatively similar production of particles, generating two or more grams of large flake-like particles, but only ∼10 mg to ∼100 mg of nanoparticles. The most efficient nanoparticle production, and largest nano/microparticle ratio resulted from milling in neat (low viscosity) acetonitrile, where more than a gram of nanopowder, along with more than a gram of micron-size flakes were produced. Given the ease with which the nano and micron scale particles can be separated by sedimentation, milling of aluminum balls in acetonitrile constitutes an efficient, inexpensive synthetic process. The efficient production of nanoparticles particles by milling with molecules expected to bind to the aluminum surface extends earlier work by Gayko et al. on Al powder milling, where they showed that surface-active solvents resulted in smaller particles, albeit in the >20 μm size range.

Consistent with the idea that a surface-active solvent enhances wear, ethanol also gave very efficient particle production; however, as discussed in the Supporting Information, the high reactivity of ethanol with aluminum lead to production of aluminum oxide particles and H_2 gas. Similarly, dichloromethane was so reactive that the product was a solution of $AlCl_3$.

For milling in reactive liquids or solutions, the initial roughness of the balls does not appear to make a significant difference in the particle production rate, presumably because material is rapidly worn from the surfaces, such that a steady state surface roughness is reached early in the milling process. Microscopy of balls recovered after milling under different conditions is discussed below.

Because acetonitrile gave the most efficient nanoparticle production, it is worth describing in more detail. Aluminum balls milled in neat acetonitrile result in formation of a dense, black slurry. To stabilize the particles and aid separation, oleic acid was added to the acetonitrile suspension and milled briefly at low speed (100 rpm), to thoroughly mix the slurry. After reaction with oleic acid, the particles precipitated out of the acetonitrile suspension, leaving a supernatant that was slightly cloudy and yellow in color, presumably reflecting the presence of impurities, including aluminum particles too small to precipitate quickly. After pouring off the supernatant, the

precipitated particles were readily dispersed in *n*-hexane, producing a dense black suspension (see Supporting Information Figure S2b). Centrifugation of this suspension was used to separate out large particles (~1 g), from the nanoparticles remaining in suspension. These were then dried, resulting in ~1 g of nanoparticles.

The nanoparticle fraction suspended in *n*-hexane was diluted and analyzed by dynamic light scattering, and Figure 1 shows

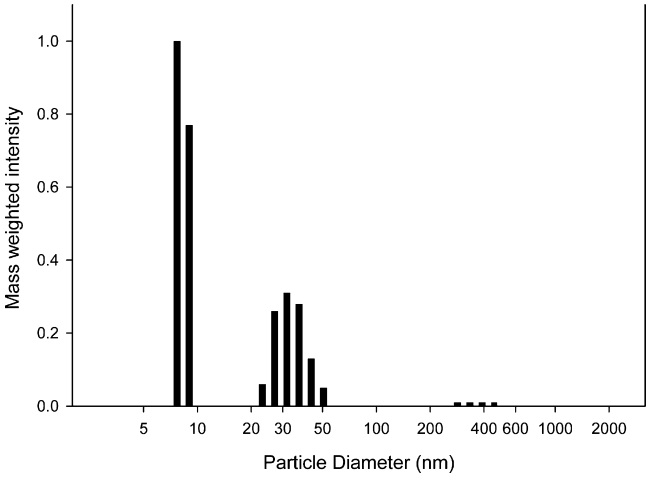

Figure 1. Dynamic light scattering analysis of aluminum nanoparticles milled in acetonitrile for 3 h, capped with oleic acid, and redispersed in *n*-hexane.

the result. As a control, DLS measurements were also performed on 5% oleic acid in *n*-hexane, confirming that oleic acid micelles were not giving rise to significant light scattering signal. The Al nanoparticle distribution is bimodal, with a sharp peak in the 5−10 nm range and with ~24% of the total mass of nanoparticles in a broader feature centered around ~35 nm. There is also weak signal for particles in 250−500 nm range, indicating the presence of a small mass fraction corresponding to either aggregates of the small particles, or large particles that were not completely eliminated in the centrifugation step. Figure 2 shows the size distribution of the large particles from the sediments collected after centrifugation, resuspended in *n*-hexane. This suspension was not very stable and was

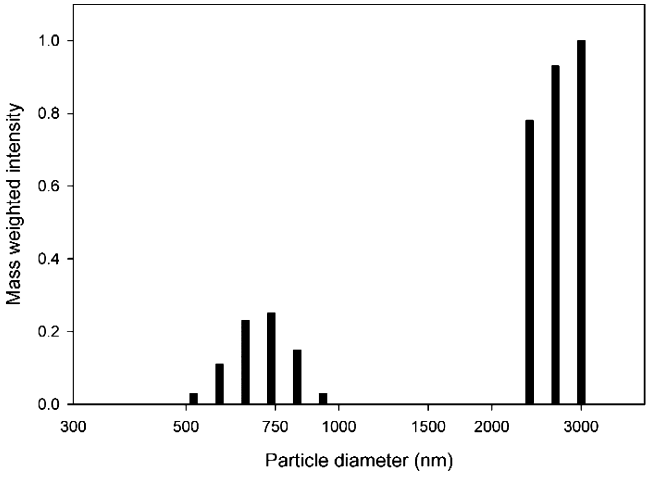

Figure 2. Dynamic light scattering analysis of the aluminum particles collected by centrifugation.

ultrasonicated just prior to DLS data collection. There is a small peak (<20 mass %) in the 500−900 nm range, but >80% of the sediment mass consisted of particles greater than two microns in size, with the distribution cut off at three microns by the DLS instrument. Microscopic analysis of the particles is discussed below.

Comparison of the results for the various solvent mixtures suggests several factors that appear to control nanoparticle production rates. It is clear that solvents such as hydrocarbons, which do not interact strongly with aluminum surfaces, are ineffective for nanoparticle production. Conversely, solvents that contain functional groups that are too reactive with aluminum (e.g., ethanol, DCM) may aid particle generation but also decompose and react with aluminum, generating salts or oxidized particles. Efficient nanoparticle production appears to require a solvent that interacts with aluminum, strongly enough to allow binding to the surfaces as they are exposed, but not so strongly that the solvent decomposes and converts the aluminum to an oxidized form. The fact that acetonitrile is efficient for nanoparticle generation, but materials such as oleic acid, oleylamine, or benzyl amine are not, unless they are diluted, suggests that viscosity may also play a role. Acetonitrile has similar viscosity to heptane (341 μPa·s vs 389 μPa·s at room temperature),[40−42] but acetonitrile is polar and has unpaired electrons on the nitrogen that might be expected to result in a significant adsorption energy on unoxidized aluminum surfaces. Oleic acid has a carboxylic acid group that clearly binds strongly to aluminum; however, its viscosity is high (>27 000 μPa·s),[34,35] as are those of oleylamine and benzylamine. Oleic-acid-capped nanoparticles can be generated by adding oleic acid to nonreactive solvents such as toluene or *n*-hexane; however, nanoparticle production is more efficient if the aluminum is first milled in neat acetonitrile, with oleic acid added later.

Because acetonitrile was particularly effective at particle production, its mode of interaction with surfaces is of interest. We were unable to find any detailed studies of acetonitrile−aluminum binding, but Schwartz and Hamers[43] used XPS and polarized infrared analysis to study acetonitrile binding to silicon, reporting that the C═N bond was predominantly parallel to the Si (001) surface. This result suggested that the dative bond initially formed between the terminal N atom and the Si surface was augmented by formation of an additional bond to either the α or β-carbon. FTIR studies by Schwartz and Hamers[44] on silicon and Filler et al.[45] on germanium found evidence for a ketenimine (C═C═N) stretch, and Schwartz and Hamers[44] also discuss the possibility of a less stable "(2 + 2)" adduct on the surface, where the α-carbon binds to the surface and results in an intact methyl group extending from the adduct (CH_3—C═N).

In the interest of better understanding the mechanism for aluminum particle production in from the parent media, microscopy was performed on the nanoparticles, the micron scale particles, and the ball surfaces before and after milling. As shown in Figure 3, the postmilling surface morphology of the balls is significantly different for different milling solvents, even when viewed at low magnification. All images show the surface of balls removed after 3 h of milling at 350 rpm, with fresh as-received balls used in each experiment, so as to avoid any residual structure from prior milling. As shown in Figure 3, more surface damage is recorded if the media are milled in a solvent or solution which has at least one component that would be expected to react with nascent elemental aluminum

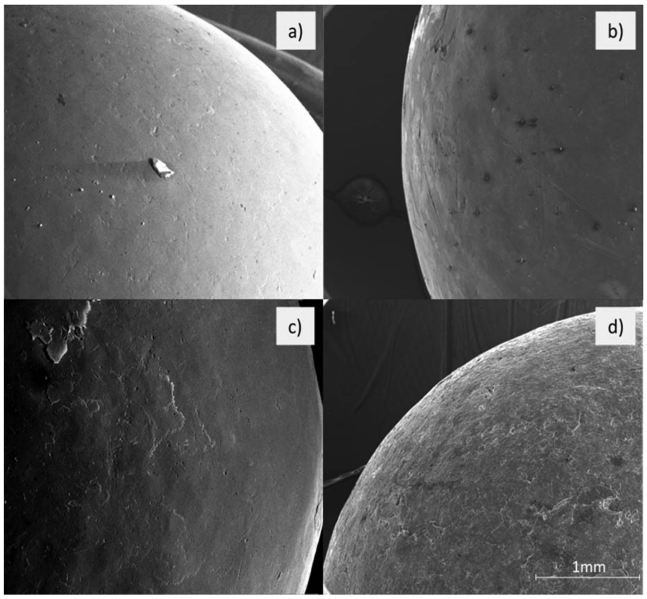

Figure 3. Scanning electron microscopy images of aluminum balls used in homogeneous media milling: (a) As-received; (b) milled 6 h in neat toluene; (c) milled 3 h in 10 mM of oleic acid in toluene; (d) milled 3 h in acetonitrile.

surfaces. If oleic acid is added to the toluene (Figure 3c), increasing particle production is observed, and as might be expected, the surface of the ball shows more signs of wear than the as-received balls (Figure 3a) or balls milled in a nonreactive solvent (toluene Figure 3b). There is significantly more pitting, as well as large (>100 μm) features that appear to be layers in the process of exfoliation, which one might expect to give rise to flake-like particles. The brightness of the edges of these features suggests differential charging from the electron beam, possibly indicating that the edges are no longer in good electrical contact with the body of the ball. It seems reasonable to assume that the micron scale flake-like particles observed in many of the milling runs result from this exfoliation process, although it is possible that some of the adhering flakes result from cold welding of previously generated flakes back to the surface of the ball.[46] It is not clear if the small number of nanoparticles generated under these conditions also are generated by flaking of micron size particles, following by grinding of the flakes into the nanoscale, or whether there is a different process for direct ejection of nanoparticles from the surface.

The transformations that can occur during severe plastic deformation are well-documented in mechanochemical literature.[47−50] These transformations can include changes in crystal structure, particle size, grain size, and particle morphology. Here, we record not only a variety in the size and morphology of the particles, but obvious changes in the parent material give further clues as to how the dislodging of particles from an amorphous parent material proceeds. Figure 3d shows a ball milled in neat acetonitrile, under conditions where roughly equal masses of large flake-like particles and nanoparticles were generated. The ball surface is much rougher and shows evidence of both pitting and exfoliation. The difference among these samples tends to suggest that flake-like particles result from exfoliation but that there may also be a process leaving pits on the ball surfaces that is correlated with efficient nanoparticle production.

Figure 4 shows a micrograph of a large flake collected after only 15 min of milling in acetonitrile. Note the evidence

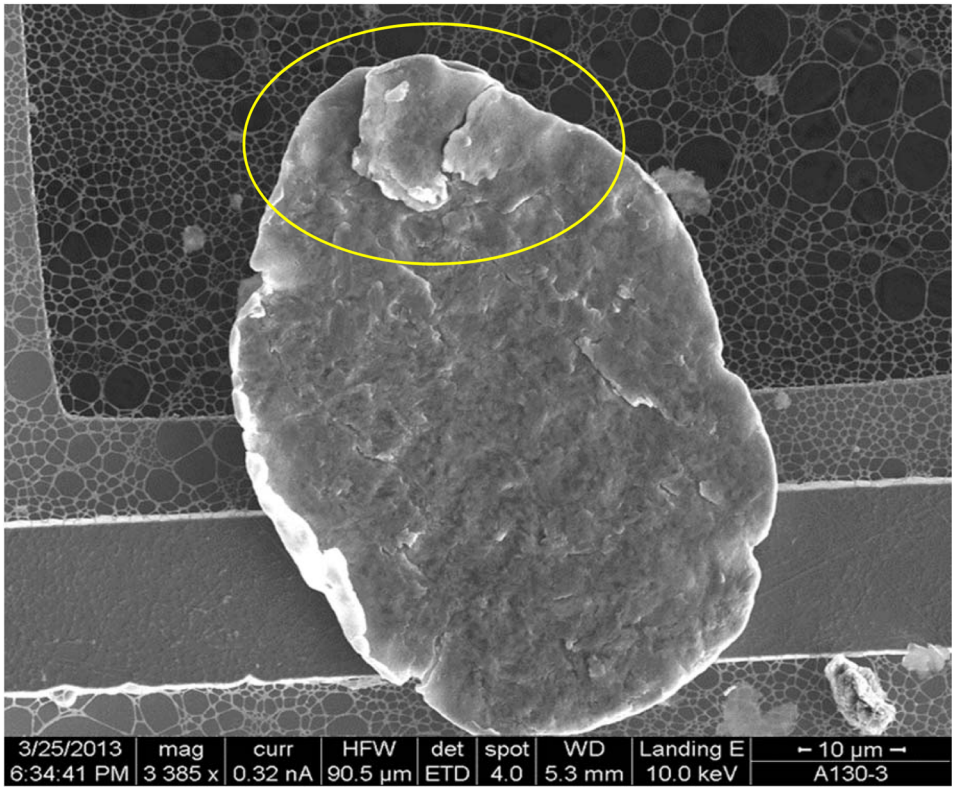

Figure 4. Scanning electron micrograph (SEM) of a large aluminum flake produced in 15 min of acetonitrile milling.

suggesting that this particle was in the process of exfoliating additional smaller flakes (circled region). The apparent curling of the left edge of the flake could be further evidence of exfoliation. Figure 5 shows nanoparticles that were extracted

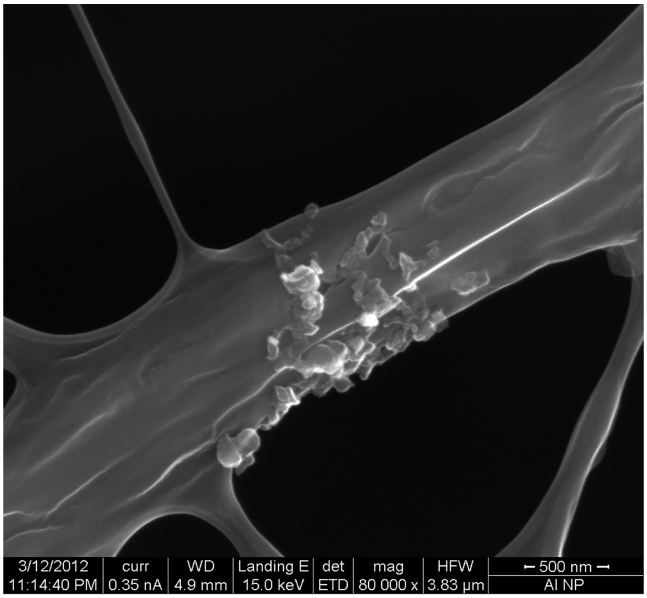

Figure 5. SEM image of acetonitrile-milled particles, subsequently capped with oleic acid, and deposited on lacey carbon.

from the particle mixture after 3 h of milling in acetonitrile, mixed with oleic acid, transferred to hexane, and then drop cast onto a TEM grid. The particle size distribution in this SEM image contains particles in the 30−200 nm size range. The main difference is that the SEM image shows no evidence of particles in the sharp DLS peak between 5−10 nm; however, such small particles of a low Z element may simply not have sufficient contrast to be resolved, particularly, given that they are coated with oleic acid. To image these smaller particles, STEM was used, as shown in Figure 6, which shows the image

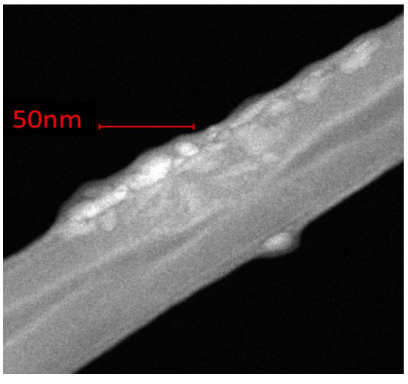

Figure 6. TEM image of acetonitrile-milled particles, subsequently capped with oleic acid, and deposited on lacey carbon.

of a group of particles, which individually have sizes below 20 nm. The faint, lighter gray layer on the surface of the particles is consistent with them being coated with an oleic acid layer. As noted, particles initially produced by milling in acetonitrile, become highly dispersible in hexane after ultrasonic mixing with oleic acid, suggesting that the carboxylic acid might be bound to the aluminum surfaces. To test this hypothesis, reflectance FTIR was performed, and Figure 7 compares the spectrum for aluminum nanoparticles capped with oleic acid (bottom), to that for neat oleic acid (top). For this experiment, the sample was washed three times with ethanol (in *n*-hexane suspension) to remove excess oleic acid. For neat oleic acid, strong absorption peaks are seen at 2854 and 2925 cm^{-1}, corresponding to the symmetric and asymmetric CH_2 stretches of the sp^2 hybridized (aliphatic) regions of the backbone, as well as a weaker feature at 3004 cm^{-1} corresponding to the olefinic CH stretch associated with the double bond in the backbone.[51] The broad feature extending from 3600 to 2400 cm^{-1} is assigned to the OH stretch, inhomogeneously broadened by hydrogen bonding in the liquid. Modes associated with the COH group are located at 1413 and 1286 cm^{-1},[52] and the most obvious peak in the fingerprint region for neat oleic acid is the (C═O) stretch at 1713 cm^{-1}.[52]

The spectrum of the nanoparticles retains the CH_2 and olefinic CH stretch peaks of the hydrocarbon tail, but the broad OH stretch band is largely absent. The OH bending mode at 1413 cm^{-1} is also absent, further suggesting that the OH group is involved in binding to the aluminum. Most importantly, the C═O stretch peak (1713 cm^{-1}) in neat oleic acid is essentially absent in the nanoparticle sample, and new peaks appear at 1608 and 1468 cm^{-1}, which are assigned to the asymmetric and symmetric stretches of the now-equivalent CO bonds in the carboxylic acid headgroup.[17,53] Involvement of both oxygen atoms in binding to the aluminum is also suggested by the absence of the COH mode at 1286 cm^{-1}.[54,55]

C^{13} solid-state NMR was performed to investigate the nature of how a simple carboxylic acid interacts with the aluminum particle surfaces. Acetic acid was used to simplify the spectrum. Particles were produced by milling in acetonitrile, then ultrasonically mixed with acetic acid, and ultrasonically washed twice with ethanol, to remove the excess acetic acid The NMR spectrum is shown in Figure S6 of the Supporting Information. Signals are observed for both the methyl- and carboxylate carbon atoms, at 21 and 178 ppm, respectively (Supporting Information Figure S6). The spectra confirm the presence of acetic acid on the surface, despite vigorous washing; however, we were unable to obtain structured spectra that might reveal the binding motif.

The FTIR and SSNMR results show that oleic or acetic acids are bound strongly enough to the aluminum surface to resist vigorous washing, and the disappearance of the OH and CO stretch absorptions in the FTIR data suggest that the carboxylic acid is bound to aluminum in such a way as to no longer have OH or free CO moieties, that is, that it is covalently bound to the aluminum. There are several binding geometries that might play a role. One is a monodentate interaction in which the OH moiety binds to aluminum, losing the H atom in the process. The IR spectrum for this binding arrangement should have a strong peak at 1713 cm^{-1} from the uncomplexed C═O group; thus, the near absence of this peak suggests that monodentate binding probably does not play a major role−not surprising given aluminum's high affinity for oxygen. It is unclear whether the residual intensity at 1713 cm^{-1} results from a small extent of monodentate binding or if there was simply some residual uncomplexed oleic acid left after repeated ethanol washing.

The other two configurations are both bidentate and differ in that one has both O atoms in the carboxylate group binding to a single aluminum atom ("chelating bidentate"), and the other has the two O atoms binding to adjacent Al atoms ("bridging

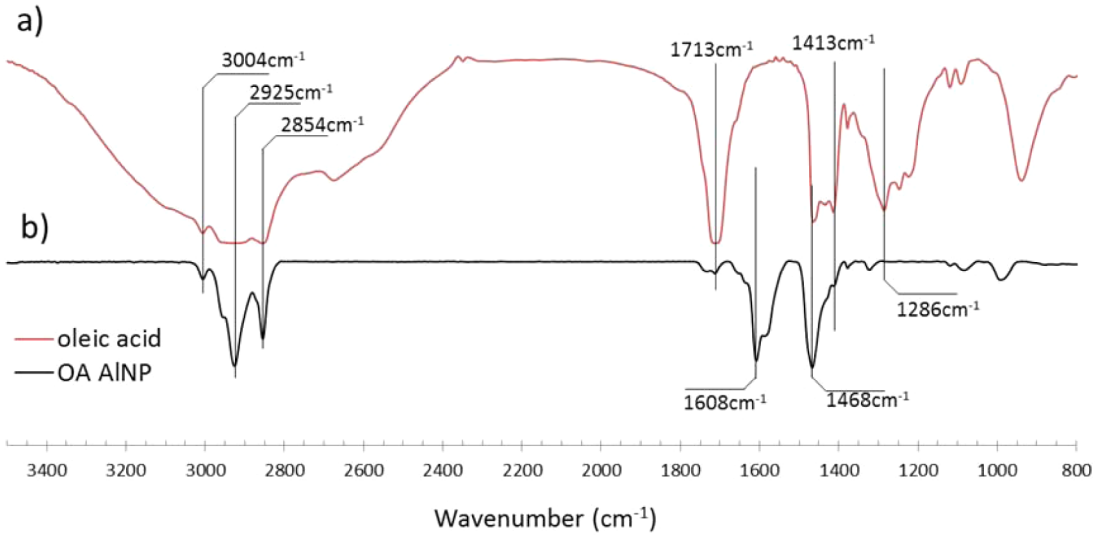

Figure 7. Reflectance FTIR of (a) neat oleic acid; (b) oleic acid-capped aluminum nanoparticles.

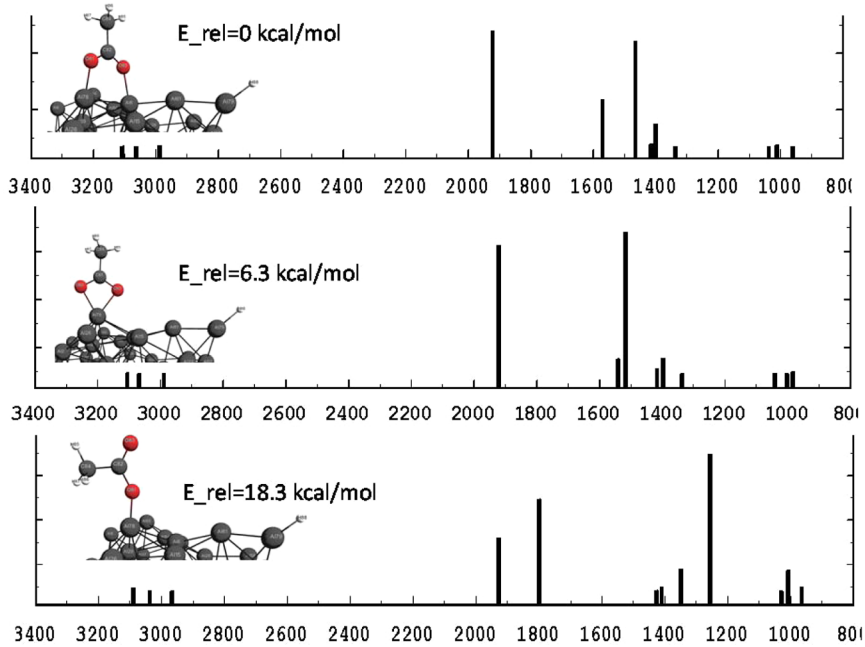

Figure 8. Calculated IR spectra for the three most stable arrangements for binding acetic acid to an Al_{80} cluster as calculated using density functional theory with a basis set of M06/6-311++G(d,p). The energies of the three structures, relative to that of the most stable bridging bidentate structure, are given.

bidentate"). Wu et al.[56] have proposed that the separation between the symmetric and asymmetric peaks CO stretching peaks can be used to distinguish between chelating and bridging bidentate bonding (for binding to cobalt). If we assume that binding to aluminum is similar, then the bridging bidentate configuration should result in asymmetric-symmetric stretch separation of 140 cm^{-1} to 190 cm^{-1}, while the chelating bidentate separation should be smaller splitting.[56] In our spectrum, the separation is 140 cm^{-1}, suggesting the bridging bidentate structure; however, there is a shoulder on the asymmetric stretch peak at 1581 cm^{-1}, and the separation of this shoulder from the symmetric stretch peak is only 105 cm^{-1}, raising the possibility that there might also be some chelating bidentate binding.[57]

To clarify this question, carboxylic acid binding to aluminum was studied using DFT, calculating the structures and energetics for acetic acid binding to the surface of an Al_{80} cluster that has both surface and bulk-like core atoms. Harmonic frequencies and infrared intensities were calculated for the bridging bidentate, chelating bidentate, and two monodentate isomers. Zero point vibrational energy corrections were applied to identify global minima, and the energies are reported with respect to that of the most isomer. The bridging bidentate arrangement is found to be most stable, with the chelating bidentate arrangement 6.3 kcal/mol higher in energy, and the two possible monodentate structures at relative energies of 18.3 kcal/mol (binding via the OH oxygen atom) and 39.7 kcal/mol (binding via the C═O oxygen atom).

The calculated IR spectra for the three most stable binding arrangements are shown in Figure 8. Figure S7 in the Supporting Information compares the experimental spectrum of oleic-acid capped aluminum nanoparticles with the DFT spectra for four possible binding arrangements. As noted, the two monodentate structures can be excluded because they should have a strong absorption for the free CO stretch, which is not seen experimentally. The calculated spectrum for the chelating bidentate structure is also in poor agreement with the experimental spectrum, showing only a single peak in the frequency range where the CO stretch modes are expected. The calculated spectrum for the bridging structure, in contrast, is in excellent agreement with experiment. The two features corresponding to the symmetric and antisymmetric stretch of the CO bonds are seen with roughly the correct intensities, as are weaker features at low frequencies. The intensity in the CH stretch range is, as expected, much weaker for the DFT spectrum of Al_{80}-acetic acid than in the experiment, with oleic acid. The one apparent discrepancy is the prominent peak calculated to appear at ∼1920 cm^{-1}, due to the Al−H stretch. The absence of such a feature in the experimental spectrum suggests that the H atoms generated by binding of the carboxylic acid group to aluminum may recombine and desorb as H_2.

To further probe binding of adsorbates to the aluminum surface and the oxidation state of the aluminum after air exposure, X-ray photoelectron spectroscopy (XPS) was used to examine samples of aluminum particles with, and without, oleic acid functionalization. Samples were dried and transferred to the XPS instrument in air, and then lightly Ar-sputtered to remove adventitious adsorbates, and implant Ar so that the Ar $2p_{3/2}$ peak at 241.9 eV could be used for energy calibration.[23] Survey scans are included in the Supporting Information (Figure S3) for both aluminum milled only in acetonitrile (lower spectrum) and aluminum milled in acetonitrile and subsequently capped with oleic acid (upper spectrum). One point of interest is that there is no detectable W, Co, Fe, or other contaminants that might arise from the Co-cemented tungsten carbide jar or stainless steel lid. Not surprisingly, the carbon 1s peak dominates for the oleic acid-capped sample, both because oleic acid contains carbon and because the presence of the capping layer attenuates signal from the underlying particle. For the uncapped sample, the dominant peak is O 1s, as expected for oxidized aluminum particles. The fact that the O 1s peak is larger than the Al 2s or 2p peaks, reflects the fact that the XPS sensitivity factor is ∼3.7 times greater for O, compared to Al.

High resolution scans over the Al 2p peaks for the two samples are shown in Figure 9. For the uncapped sample (Figure 9a), the spectrum is dominated by a high binding energy peak centered at 74.5 eV, which corresponds to Al in some oxidized form.[17,58−61] There is also a weak shoulder at lower binding energies, which is attributed to unoxidized Al in the core of the particles. The 72.0 eV binding energy for this feature is lower than expected for bulk aluminum (72.9 eV), but there is considerable uncertainty due to the weakness of the feature. The form of the oxidized aluminum is not clear, but obvious possibilities are aluminum bound to oxygen and/or nitrogen (from acetonitrile). For example, the 74.5 eV peak energy is within the ranges reported for both AlN and Al_2O_3.[23,58,61−63]

In the spectrum for the oleic acid-capped sample (Figure 9b), several points are obvious. There is roughly factor of 3

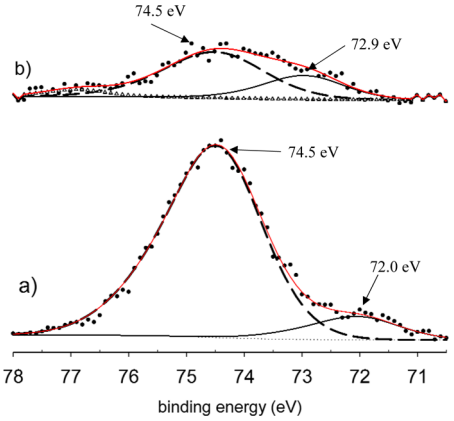

Figure 9. High resolution scans of the Al 2p peak for (a) acetonitrile-milled aluminum nanoparticles; (b) acetonitrile-milled, oleic acid-capped aluminum nanoparticles. Note: both samples were argon sputtered to remove adventitious species.

attenuation of the integrated aluminum signal, compared to that in the uncapped sample, as expected due to scattering of aluminum photoelectrons as they pass through the oleic acid layer. The spectrum for capped aluminum particles also shows features for oxidized (74.5 eV) and unoxidized aluminum (72.9 eV), but clearly, the relative intensity for the oxidized aluminum is lower. For the uncapped spectrum the oxidized/unoxidized integrated intensity ratio is ∼ 9:1, dropping to ∼ 2.5:1 for the capped sample, indicating that oleic acid is at least partially passivating the particles with respect to air oxidation. As noted above, the 74.5 eV "oxidized" feature may include contributions from aluminum bound to both N and O, and the latter is at least partially due to binding of oleate to the aluminum surface.

Figure S7 in the Supporting Information shows the distribution of Al 2p binding energies estimated using orbital energies from the DFT calculations. Distributions are shown for the Al_{80} cluster, and for Al_{80} with a single acetic acid molecule bound in the three arrangements shown in Figure 8. Because the DFT model system included only a single ligand molecule and the estimation method does not include final state relaxation effect, the results are not directly comparable to experiment; however, they do show that binding of a single carboxylate leads to significant broadening of the Al 2p binding energy distribution. In particular, the one or two Al atoms involved in Al−O bonds are those with the highest binding energies, as expected.

High resolution scans for the C 1s and N 1s regions are shown in Figures S4 and S5 of the Supporting Information. For the uncapped sample, the C 1s spectrum is broad and weak (note ×10 scaling). The carbon in this spectrum must originate from the acetonitrile used in milling and adventitious carbonaceous molecules. For the oleic acid-capped sample, the C 1s intensity is much greater, as expected, and the spectrum is dominated by a peak at 285 eV, which is assigned to carbon in the oleate layer. Because of unknown contributions from adventitious sources, more detailed assignment is not warranted. The N 1s spectra show that there is detectable nitrogen in both samples and that neither the spectral features nor their intensities are strongly affected by capping. The main peak near 399 eV is consistent with organic nitrogen and could result either from bound acetonitrile or adventitious molecules. The weaker ∼397 eV feature is in the range expected for metal nitrides. Note, however, that if either of the N 1s features arises

from N bound to the aluminum particles, we would expect that feature to be attenuated in the oleic acid-capped sample. The fact that the two spectra are so similar suggests that much of the nitrogen signal arises from adventitious sources and therefore that nitride formation is probably not a significant contributor to the oxidized aluminum signal in Figure 9.

Figure 10 shows high resolution scans over the O 1s regions for both samples. The fact that the O 1s intensity is much

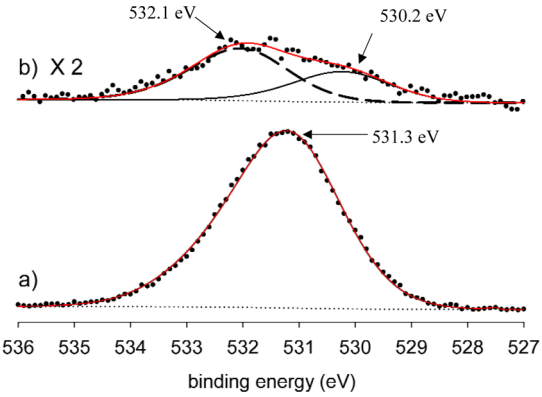

Figure 10. High resolution scans of the O 1s peak for (a) acetonitrile-milled aluminum nanoparticles; (b) acetonitrile-milled, oleic acid-capped aluminum nanoparticles. Note: both samples were argon sputtered to remove adventitious species.

weaker in the capped sample (note ×2 scale factor) results from two factors. As shown by the Al 2p results in Figure 9, the aluminum in the capped sample is substantially less oxidized than in the uncapped sample. In addition, signal from oxygen present on the aluminum surfaces would be attenuated by passage through the capping layer. For the uncapped sample, the spectrum is well fit by a single peak centered at 531.3 eV, which is assigned to aluminum oxide (Al_2O_3)[64,65] The O 1s spectrum for the capped sample has contributions from at least two components, which is not surprising given that there may be oxygen from binding of oleate to the surface, from O_2 oxidation of the aluminum surface, and from adventitious sources.

In summary, the XPS results are consistent with binding of an oleate layer to the aluminum particle surfaces, which at least partially passivates the particles with respect to further oxidation upon air exposure. The XPS data also suggest that formation of either aluminum nitride or carbide during milling acetonitrile is not significant.

4.2. Synthesis of Iron and Iron Oxide Nanoparticles. To investigate the generality of the method, similar experiments were done for iron, that is, a significantly harder, but still ductile metal. Iron nanoparticles were produced by milling steel balls in a 5% solution of oleic acid in *n*-hexane in Ar atmosphere. The resulting particles form a dense black suspension, which is stable with respect to settling out for at least 6 months. The size distribution was analyzed by DLS, and the mass-weighted (i.e., volume-weighted) results are given in Figure 11. The distribution is dominated by a peak in the 10−20 nm size range, and there is also a small component peaking near 600 nm, with essentially no signal for particles in the range between 20 and 400 nm. It is not clear if the 600 nm particles are aggregates of the small primary particles or if there are simply a few large particles present. In any case, their contribution to the particle distribution would only be a few parts per million on a

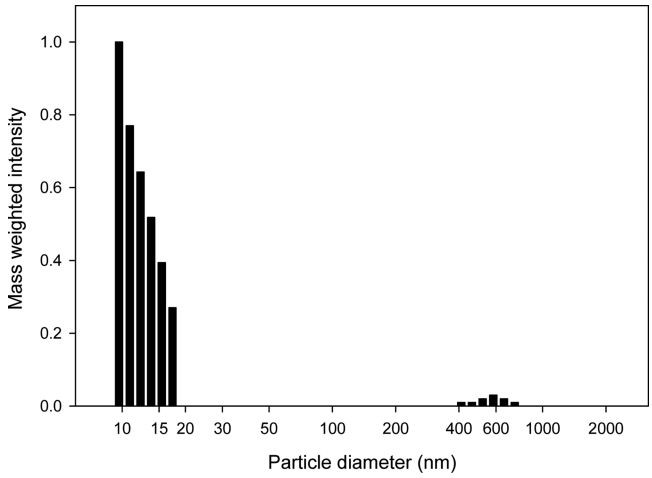

Figure 11. Mass weighted particle size distribution for oleic acid-capped iron nanoparticles synthesized by milling for 3 h in 5% oleic acid/hexanes under an argon atmosphere.

number-weighted basis, and if desired, they can easily be separated out by centrifugation. Electron microscopy was used to investigate the particle morphology, as described in the Supporting Information (Figure S9 and S10, and associated text), resulting in particle sizes in reasonable agreement with the DLS results.

To confirm that oleic acid was actually binding to the iron, FTIR experiments analogous to those done for aluminum are reported in Figure S11 and associated discussion in the Supporting Information. As in the aluminum case, the spectrum of washed particles shows modes associated with CH stretches in the hydrocarbon tail, and for carboxylate CO stretches, but no significant intensity for OH or free C═O, suggesting that a bidentate interaction is dominant.

X-ray photoelectron spectroscopy was employed to look at the oxidation state of the different preparations of the iron nanoparticles. Supporting Information Figure S12 shows survey spectra for both (a) argon-milled and (b) air-milled iron nanoparticles, both also milled with oleic acid and then ethanol-washed repeatedly to remove excess oleic acid. Supporting Information Figure S13 shows the Fe $2p_{3/2}$ peak structure in more detail. Both sets of spectra are consistent with the air-milled sample being substantially oxidized, while the sample milled under Ar shows mostly metallic iron, along with smaller signal for partially oxidized iron which we attribute to binding of oleate to the iron surfaces.

4.3. Copper Nanoparticles. The experiments with copper provide another example of a ductile, malleable metal but also test the necessity of using spherical milling media. Because we were unable to obtain copper balls at reasonable cost, we used 1:1 aspect ratio copper cylinders. Copper particles were produced using conditions that also resulted in reasonable production of particles for aluminum and iron. Copper cylinders (200 g) were milled with 100 mL of a 5% (0.16 M) solution of oleic acid in hexanes, at 350 rpm for 3 h. The result was a copper-colored product containing approximately 15 g of particles, many of which were in the >100 μm size range, easily seen with the naked eye. The large particles rapidly sedimented out of suspension, leaving a dense suspension of smaller particles, which still appeared copper-colored, indicating the presence of particles in micron size range. These initial suspensions were stable for at least 1 h, but upon

centrifugation, could be separated further into particles in the few micron range, which settled out, and a dense black suspension of nanoparticles (Supporting Information Figure S14a). DLS was used to probe this centrifuged nanoparticle suspension, resulting in a bimodal size distribution with one component centered at ∼250 nm, making up ∼7% of the total particle mass, with the remaining mass represented by a distribution centered at ∼900 nm.

In the nitrogen glovebox, the suspended nanoparticles were stable for more than a week, but upon exposure of the suspensions to air, they quickly (<20 min) converted to a clear blue solution which we attribute to formation Cu^{2+}, dissolved in hexane, presumably via interaction with oleic acid (Supporting Information Figure S14b). The conversion is surprisingly rapid, as shown by Figure S15 (Supporting Information), which gives a time history for dissolution of a dense suspension containing both nano- and micro-Cu particles. Since the suspensions are stable in hexanes in absence of air, it is clear that the copper particles are initially complexed by oleic acid. The rapid dissolution shows that the oleate layer does not passivate the surfaces against oxidation by atmospheric oxygen diffusing into the *n*-hexane solvent.

5. CONCLUSION

This milling method has the capacity to produce nanoparticles on the gram scale from inexpensive media. It is not possible to determine the mechanism of particle production in detail, but several aspects of the mechanism appear clear. The strong dependence of particle production on the nature of the milling solvent or solution, indicates that interaction between the metal surfaces and the solvent or solutes, is critical to particle production. In particular, particle production requires the presence of molecules, which are able to bind to the metal surface, lowering the surface free energy as cracks propagate, and presumably inhibiting cold welding. High viscosity appears to inhibit production, particular of the nanoparticle fraction of the total particle mixture. For aluminum, microscopic examination of both the particles produced under various milling conditions, and the surfaces of the balls suggests that one mode of particle production involves exfoliation of flakes of materials, which may be further broken up by milling. The more extensive pitting of the balls under conditions where nanoparticle production is high suggests that there may also be a second mechanism that correlates with nanoparticle generation.

From the perspective of the mechanism for nanoparticle production, it is useful to consider the full size distribution for aluminum milled in acetonitrile, under conditions where both nanoparticles and micron-scale flakes are generated in roughly equal amounts. The nanoparticle portion of the distribution consists mainly of particles in the 5 to 10 and 20 to 50 nm size ranges, with much weaker signal (24% of the nanoparticle mass) in the 250 to 500 nm range. DLS of the large particles sedimented out of the initial distribution shows a small feature in the 500 to 900 nm range, but the bulk of the large particles are flake-like, and larger than 2 μm, as confirmed by SEM analysis. If the only mechanism for nanoparticle production were breaking up large flakes, one might expect that the size distribution should be more continuous than the observed distribution, where there is a large gap with negligible particle mass between 50 and 250 nm, and a smaller gap between 900 nm and 2.5 μm.

In summary, the distribution of particles produced by reactant-assisted mechanical attrition is expected to reflect a balance between wear processes that spall or abrade particles from the media surfaces, and cold welding, which tends to build up larger particles and reattach particles to the media surfaces. Though strict control of the size distribution is not upheld, gram-scale quantities of particles <500 nm is demonstrated for aluminum and iron. Being inexpensive and likely easily scalable, this method offers a high throughput technique for making copious particles for applications do not require strict size control (e.g., propulsion additives, pyrotechnics, cosmetics) Binding of surface-active molecules to the media surfaces enhances the net wear rate, indicating that the effects of adsorption on surface free energy and cold welding, outweigh any lubricating effect that might be expected from binding of molecules like oleic acid to the surface. The SEM images suggest that at least for the micron size flakes, exfoliation may occur by gradual separation as the crack between the flake and media surface propagates under repeated impacts. In that case, the presence of molecules that bind strongly to the nascent surfaces may substantially enhance exfoliation by coating the inner surfaces of the propagating crack, reducing the free energy of the crack surfaces and the propensity for subsequent impacts to cold-weld the crack shut. The same effect would presumably help nascent particles avoid being welded together to increase particle size and being welded back onto the surface of the media.

■ ASSOCIATED CONTENT

Ⓢ Supporting Information

Additional XPS, FTIR, and electron microscopy data are presented, along with a schematic of the milling jar lid, additional DFT computational results, and photographs of various particle suspensions, and the reaction of copper particles with air. This material is available free of charge via the Internet at http://pubs.acs.org.

■ AUTHOR INFORMATION

Corresponding Author

*Tel: +1 801-585-7289. E-mail: anderson@chem.utah.edu.

Author Contributions

§J.A.B. and S.L.A. are senior authors.

Funding

The Utah authors acknowledge support from the Air Force Office of Scientific Research under AFOSR MURI Grant FA9550-08-1-0400 and BRI Grant FA9550-12-1-0481.

Notes

The authors declare no competing financial interest.

■ ACKNOWLEDGMENTS

SEM and XPS were done using University of Utah shared facilities of the Micron Microscopy Suite, and STEM was done at CAMCOR, which is supported by a combination of federal and state funding. The AFRL group would like to acknowledge the Department of Defense High Performance Computing Modernization Program at the Air Force Research Laboratory, Army Research Laboratory, Engineer Research and Development Center, Maui High Performance Computing Center, and Navy DoD Supercomputing Resource Centers for computer time. Solid-state nuclear magnetic resonance was conducted by M. Larsen and P. Flynn at the University of Utah.

REFERENCES

(1) Van Devener, B.; Perez, P.; Jankovich, J.; Anderson, S. Oxide-Free, Catalyst-Coated, Fuel-Soluble, Air-Stable Boron Nanopowder as Combined Combustion Catalyst and High Energy Density Fuel. *Energy Fuels* **2009**, *23*, 6111−6120.

(2) Can, M. M.; Ozcan, S.; Ceylan, A.; Firat, T. Effect of Milling Time on the Synthesis of Magnetite Nanoparticles by Wet Milling. *Mater. Sci. Eng., B* **2010**, *172*, 72−75.

(3) Bonetti, E.; Bianco, L. D.; Pasquini, L.; Sampaolesi, E. Thermal Evolution of Ball Milled Nanocrystalline Iron. *Nanostruct. Mater.* **1999**, *12*, 685−688.

(4) Suryanarayana, C. Mechanical Alloying and Milling. *Prog. Mater. Sci.* **2000**, *46*, 1−184.

(5) Eckert, J. Relationships Governing the Grain Size of Nanocrystalline Metals and Alloys. *Nanostruct. Mater.* **1995**, *6*, 413−416.

(6) Hebda, M.; Gądek, S.; Kazior, J. Thermal Characteristics and Analysis of Pyrolysis Effects During the Mechanical Alloying Process of Astaloy Crm Powders. *J. Therm. Anal. Calorim.* **2012**.

(7) Gutman, E. M. *Mechanochem. Mat.*; Cambridge International Science Publishing: Cambridge, 1998;.

(8) Chen, L.-H.; Huang, C.-C.; Lien, H.-L. Bimetallic Iron−Aluminum Particles for Dechlorination of Carbon Tetrachloride. *Chemosphere* **2008**, *73*, 692−697.

(9) Yetter, R. A.; Risha, G. A.; Son, S. F. Metal Particle Combustion and Nanotechnology. *Proceedings of the Combustion Institute* **2009**, *32*, 1819−1838.

(10) Balaz, P.; Achimovicova, M.; Balaz, M.; Billik, P.; Cherkezova-Zheleva, Z.; Criado, J. M.; Delogu, F.; Dutkova, E.; Gaffet, E.; Gotor, F. J.; Kumar, R.; Mitov, I.; Rojac, T.; Senna, M.; Streletskii, A.; Wieczorek-Ciurowa, K. Hallmarks of Mechanochemistry: From Nanoparticles to Technology. *Chem. Soc. Rev.* **2013**, *42*, 7571−7637.

(11) Rehbinder, P. A., Reports at the Vi Conference of Russian Physicists. 1928.

(12) Ryou, J. Improvement on Reactivity of Cementitious Waste Materials by Mechanochemical Activation. *Mater. Lett.* **2004**, *58*, 903−906.

(13) Ding, H.; Zhou, H.; Zheng, Y. X.; Wang, M. M. Effect of Sodium Stearate on Grinding Behaviour of Calcium Carbonate in Wet Stirred Mill. *Mater. Res. Innovations* **2013**, *17*, 292−296.

(14) Westbrook, J. H.; Conrad, H.; Metals, A. S. f. *The Science of Hardness Testing and Its Research Applications*. American Society for Metals: 1973;.

(15) Gayko, M.; Wuestefeld, B.; Wochnowski, H. Effect of Sorption and Reaction Processes on the Strength of Metals and the Effect of Sorptively Generated Tribologic Properties on the Kinetics of Comminution. *Z. Phys. Chem. (Frankfurt am Main)* **1973**, *87*, 82−93.

(16) Lee, S. Y.; Harris, M. T. Surface Modification of Magnetic Nanoparticles Capped by Oleic Acids: Characterization and Colloidal Stability in Polar Solvents. *J. Colloid Interface Sci.* **2006**, *293*, 401−408.

(17) Lewis, W. K.; Rosenberger, A. T.; Gord, J. R.; Crouse, C. A.; Harruff, B. A.; Fernando, K. A. S.; Smith, M. J.; Phelps, D. K.; Spowart, J. E.; Guliants, E. A.; Bunker, C. E. Multispectroscopic (Ftir, Xps, and Tofms-Tpd) Investigation of the Core-Shell Bonding in Sonochemically Prepared Aluminum Nanoparticles Capped with Oleic Acid. *J. Phys. Chem. C* **2010**, *114*, 6377−6380.

(18) Guardia, P.; Labarta, A.; Batlle, X. Tuning the Size, the Shape, and the Magnetic Properties of Iron Oxide Nanoparticles. *J. Phys. Chem. C* **2010**, *115*, 390−396.

(19) Jeng, J. Y.; Liu, J. C.; Jean, J. H. Dispersion of Oleate-Modified Cuo Nanoparticles in a Nonpolar Solvent. *J. Am. Ceram. Soc.* **2007**, *90*, 3676−3679.

(20) Bunker, C. E.; Karnes, J. J. Low-Temperature Stability and High-Temperature Reactivity of Iron-Based Core-Shell Nanoparticles. *J. Am. Chem. Soc.* **2004**, *126*, 10852−10853.

(21) Gan, Y.; Lim, Y. S.; Qiao, L. Combustion of Nanofluid Fuels with the Addition of Boron and Iron Particles at Dilute and Dense Concentrations. *Combust. Flame* **2012**, *159*, 1732−1740.

(22) Beloni, E.; Hoffmann, V. K.; Dreizin, E. L. Combustion of Decane-Based Slurries with Metallic Fuel Additives. *J. Propul. Power* **2008**, *24*, 1403−1411.

(23) Moulder, J. F.; Stickle, W. F.; Sobol, P. E.; Bomben, K. D. *Handbook of X-Ray Photoelectron Spectroscopy*. Perkin-Elmer Corporation Eden Prairie, 1992; p 261.

(24) Frydman, E.; Cohen, H.; Maoz, R.; Sagiv, J. Monolayer Damage in Xps Measurements as Evaluated by Independent Methods. *Langmuir* **1997**, *13*, 5089−5106.

(25) Hanumantha, P. J.; Datta, M. K.; Kadakia, K. S.; Hong, D. H.; Chung, S. J.; Tam, M. C.; Poston, J. A.; Manivannan, A.; Kumta, P. N. A Simple Low Temperature Synthesis of Nanostructured Vanadium Nitride for Supercapacitor Applications. *J. Electrochem. Soc.* **2013**, *160*, A2195−A2206.

(26) Zhao, Y.; Truhlar, D. G. The M06 Suite of Density Functionals for Main Group Thermochemistry, Thermochemical Kinetics, Noncovalent Interactions, Excited States, and Transition Elements: Two New Functionals and Systematic Testing of Four M06-Class Functionals and 12 Other Functionals. *Theor. Chem. Acc.* **2008**, *120*, 215−241.

(27) McLean, A. D.; Chandler, G. S. Contracted Gaussian Basis Sets for Molecular Calculations. I. Second Row Atoms, Z = 11−18. *J. Chem. Phys.* **1980**, *72*, 5639−48.

(28) Francl, M. M.; Pietro, W. J.; Hehre, W. J.; Binkley, J. S.; Gordon, M. S.; DeFrees, D. J.; Pople, J. A. Self-Consistent Molecular Orbital Methods. Xxiii. A Polarization-Type Basis Set for Second-Row Elements. *J. Chem. Phys.* **1982**, *77*, 3654−65.

(29) Clark, T.; Chandrasekhar, J.; Spitznagel, G. W.; Schleyer, P. v. R. Efficient Diffuse Function-Augmented Basis Sets for Anion Calculations. III. The 3-21 + G Basis Set for First-Row Elements, Lithium to Fluorine. *J. Comput. Chem.* **1983**, *4*, 294−301.

(30) Krishnan, R.; Binkley, J. S.; Seeger, R.; Pople, J. A. Self-Consistent Molecular Orbital Methods. Xx. A Basis Set for Correlated Wave Functions. *J. Chem. Phys.* **1980**, *72*, 650−4.

(31) Perez, J. P. L.; McMahon, B. W.; Yu, J.; Schneider, S.; Boatz, J. A.; Hawkins, T. W.; McCrary, P. D.; Flores, L. A.; Rogers, R. D.; Anderson, S. L., Boron Nanoparticles with High Hydrogen Loading: Mechanism for B-H Binding and Potential for Improved Combustibility and Specific Impulse. *ACS Appl. Mater. Interfaces* **in press**.

(32) Schmidt, M. W.; Baldridge, K. K.; Boatz, J. A.; Elbert, S. T.; Gordon, M. S.; Jensen, J. H.; Koseki, S.; Matsunaga, N.; Nguyen, K. A. et, a., General Atomic and Molecular Electronic Structure System. *J. Comput. Chem.* **1993**, *14*, 1347−63.

(33) Bowmaker, G. A. Solvent-Assisted Mechanochemistry. *Chem. Commun. (Camb)* **2013**, *49*, 334−48.

(34) Valeri, D.; Meirelles, A. J. A. Viscosities of Fatty Acids, Triglycerides, and Their Binary Mixtures. *J. Am. Oil Chem. Soc.* **1997**, *74*, 1221−1226.

(35) Lide, D. R. *Crc Handbook of Chemistry and Physics, Internet Version 2005*. CRC Press: Boca Raton, FL, 2005;.

(36) Mori, H.; Mio, H.; Kano, J.; Saito, F. Ball Mill Simulation in Wet Grinding Using a Tumbling Mill and Its Correlation to Grinding Rate. *Powder Technol.* **2004**, *143−144*, 230−239.

(37) Bhushan, B. *Handbook of Micro/Nano Tribology*, Second *Edition*. Taylor & Francis: 1998;.

(38) Anghel, V.; Cann, P. M.; Spikes, H. A., Direct Measurement of Boundary Lubricating Films. In *Tribol. Ser.*, Dowson, D., Ed. Elsevier: 1997; Vol. *32*, pp 459−466.

(39) El-Shall, H.; Somasundaran, P. Physico-Chemical Aspects of Grinding: A Review of Use of Additives. *Powder Technol.* **1984**, *38*, 275−293.

(40) Ibuki, K.; Nakahara, M. Temperature and Solvent Effects on Viscosity B Coefficients. Monovalent Ions in Acetonitrile at 15, 25, and 35 °C. *J. Phys. Chem.* **1990**, *94*, 8370−8373.

(41) Dymond, J. H.; Oye, H. A. Viscosity of Selected Liquid N-Alkanes. *J. Phys. Chem. Ref. Data* **1994**, *23*, 41−53.

(42) de Heer, W. A. The Physics of Simple Metal Clusters: Experimental Aspects and Simple Models. *Rev. Mod. Phys.* **1993**, *65*, 611−76.

(43) Schwartz, M. P.; Hamers, R. J. Reaction of Acetonitrile with the Silicon (001) Surface: A Combined Xps and Ftir Study. *Surf. Sci.* **2007**, *601*, 945−953.
(44) Schwartz, M. P.; Hamers, R. J. The Role of Pi-Conjugation in Attachment of Organic Molecules to the Silicon (001) Surface. *Surf. Sci.* **2002**, *515*, 75−86.
(45) Filler, M. A.; Mui, C.; Musgrave, C. B.; Bent, S. F. Competition and Selectivity in the Reaction of Nitriles on Ge(100)-2 × 1. *J. Am. Chem. Soc.* **2003**, *125*, 4928−4936.
(46) Zhu, Y.-G.; Li, Z.-Q.; Zhang, D.; Tanimoto, T. Structural Changes in Poly(Ethylene Terephthalate) Induced by Cryomilling and Ambimilling. *J. Polym. Sci., Part B: Polym. Phys.* **2006**, *44*, 986−993.
(47) Gertsman, V. Y.; Valiev, R. Z.; Akhmadeev, N. A.; Mishin, O. V. Deformation Behavior of Ultrafine-Grained Materials. *Mater. Sci. Forum* **1996**, *225−227*, 739−744.
(48) Mishin, O. V.; Gertsman, V. Y.; Valiev, R. Z.; Gottstein, G. Grain Boundary Distribution and Texture in Ultrafine-Grained Copper Produced by Severe Plastic Deformation. *Scr. Mater.* **1996**, *35*, 873−878.
(49) Zhang, X.; Wang, H.; Kassem, M.; Narayan, J.; Koch, C. C. Preparation of Bulk Ultrafine-Grained and Nanostructured Zn, Al and Their Alloys by in Situ Consolidation of Powders During Mechanical Attrition. *Scripta Materialia* **2002**, *46*, 661−665.
(50) Jang, J. S. C.; Koch, C. C. Amorphization and Disordering of the Nickel-Aluminum (Ni3al) Ordered Intermetallic by Mechanical Milling. *J. Mater. Res.* **1990**, *5*, 498−510.
(51) Chen, S.; Liu, W. Oleic Acid Capped Pbs Nanoparticles: Synthesis, Characterization and Tribological Properties. *Mater. Chem. Phys.* **2006**, *98*, 183−189.
(52) Robinet, L.; Corbeil, M. C. The Characterization of Metal Soaps. *Stud. Conserv.* **2003**, *48*, 23−40.
(53) Lee, H. M.; Choi, S.-Y.; Yun, J.-Y. Preparation of Aluminum−Organic Nanocomposite Materials Via Wet Chemical Process. *Adv. Powder Technol.* **2011**, *22*, 608−612.
(54) Hou, Y.; Kondoh, H.; Shimojo, M.; Sako, E. O.; Ozaki, N.; Kogure, T.; Ohta, T. Inorganic Nanocrystal Self-Assembly Via the Inclusion Interaction of B-Cyclodextrins: Toward 3d Spherical Magnetite. *J. Phys. Chem. B* **2005**, *109*, 4845−4852.
(55) Thistlethwaite, P. J.; Hook, M. S. Diffuse Reflectance Fourier Transform Infrared Study of the Adsorption of Oleate/Oleic Acid onto Titania. *Langmuir* **2000**, *16*, 4993−4998.
(56) Wu, N.; Fu, L.; Su, M.; Aslam, M.; Wong, K. C.; Dravid, V. P. Interaction of Fatty Acid Monolayers with Cobalt Nanoparticles. *Nano Lett.* **2004**, *4*, 383−386.
(57) Bronstein, L. M.; Huang, X.; Retrum, J.; Schmucker, A.; Pink, M.; Stein, B. D.; Dragnea, B. Influence of Iron Oleate Complex Structure on Iron Oxide Nanoparticle Formation. *Chem. Mater.* **2007**, *19*, 3624−3632.
(58) Baker, C. C.; Ceylan, A.; Shah, S. I. Reactive Gas Condensation Synthesis of Aluminum Nitride Nanoparticles. *J. Nanosci. Nanotechnol.* **2006**, *6*, 146−150.
(59) Fu, Q.; Wagner, T. Interaction of Nanostructured Metal Overlayers with Oxide Surfaces. *Surf. Sci. Rep.* **2007**, *62*, 431−498.
(60) Davies, P. R.; Newton, N. G. The Chemisorption and Decomposition of Pyridine and Ammonia at Clean and Oxidised Al(111) Surfaces. *Surf. Sci.* **2003**, *546*, 149−158.
(61) Schoser, S.; Bräuchle, G.; Forget, J.; Kohlhof, K.; Weber, T.; Voigt, J.; Rauschenbach, B. Xps Investigation of Aln Formation in Aluminum Alloys Using Plasma Source Ion Implantation. *Surf. Coat. Technol.* **1998**, *103−104*, 222−226.
(62) Zähr, J.; Oswald, S.; Türpe, M.; Ullrich, H. J.; Füssel, U. Characterisation of Oxide and Hydroxide Layers on Technical Aluminum Materials Using Xps. *Vacuum* **2012**, *86*, 1216−1219.
(63) Kwon, Y.-S.; Gromov, A. A.; Ilyin, A. P.; Rim, G.-H. Passivation Process for Superfine Aluminum Powders Obtained by Electrical Explosion of Wires. *Appl. Surf. Sci.* **2003**, *211*, 57−67.
(64) Kloprogge, J. T.; Duong, L. V.; Wood, B. J.; Frost, R. L. Xps Study of the Major Minerals in Bauxite: Gibbsite, Bayerite and (Pseudo-)Boehmite. *J. Colloid Interface Sci.* **2006**, *296*, 572−576.
(65) Balchev, I.; Minkovski, N.; Marinova, T.; Shipochka, M.; Sabotinov, N. Composition and Structure Characterization of Aluminum after Laser Ablation. *Mater. Sci. Eng., B* **2006**, *135*, 108−112.